Nano Energy (2015) 12, 612–625

Available online at www.sciencedirect.com

ScienceDirect

journal homepage: www.elsevier.com/locate/nanoenergy

RAPID COMMUNICATION

Ultrathin supercapacitor electrodes with high volumetric capacitance and stability using direct covalent-bonding between pseudocapacitive nanoparticles and conducting materials

Yongmin Ko[a], Dongyeeb Shin[a], Bonkee Koo[a], Seung Woo Lee[b], Won-Sub Yoon[c,*], Jinhan Cho[a,*]

[a]*Department of Chemical and Biological Engineering, Korea University, Anam-dong, Seongbuk-gu, Seoul 136-713, Republic of Korea*
[b]*School of Mechanical Engineering, Georgia Institute of Technology, Atlanta, Georgia 30332-0245, United States*
[c]*Department of Energy Science (DOES), Sungkyunkwan University, Jangan-gu, Suwon 440-746, Republic of Korea*

Received 16 October 2014; received in revised form 15 December 2014; accepted 1 January 2015
Available online 10 January 2015

KEYWORDS
Direct covalent-bonding;
Ultrathin supercapacitor;
Multilayers;
Amine-functionalized multiwall carbon nanotube;
Oleic acid-stabilized transition metal oxide;
Layer-by-layer assembly

Abstract
We introduce high-performance ultrathin supercapacitor electrodes obtained through the direct covalent-bonding layer-by-layer (LbL) assembly (or ligand-exchange LbL assembly) of amine-functionalized multiwalled carbon nanotubes (CNTs) and transition metal oxide nanoparticles (TMO NPs). The main characteristic of our approach is that the internal interfacial resistance of the electrodes can be minimized through the direct covalent-bonding adsorption of densely packed, high-quality TMO NPs onto CNTs without the aid of nonactive binders or insulating NP ligands, and the resulting volumetric capacitance and cycling stability of the electrodes can be significantly enhanced. For this study, well-defined oleic acid-stabilized pseudocapacitive metal oxide nanoparticles (i.e., OA-Fe_3O_4 and OA-MnO NPs) prepared in toluene were densely adsorbed onto the CNT layer due to the high affinity between the surface of the TMO NPs and the NH_2 moieties of the CNTs. The (CNT/OA-Fe_3O_4 NP)$_{20}$ multilayer electrode exhibited a high volumetric capacitance of 248 ± 15 F cm^{-3} (128 ± 7 F g^{-1}) at 5 mV s^{-1} despite the intrinsically low specific capacitance of the Fe_3O_4 NPs. Additionally,

*Corresponding authors.
E-mail addresses: wsyoon@skku.edu (W.-S. Yoon), jinhan71@korea.ac.kr (J. Cho).

http://dx.doi.org/10.1016/j.nanoen.2015.01.002

these film electrodes exhibited high performance stability, maintaining 99.2% of their initial capacitance after 1000 cycles. Furthermore, upon the insertion of OA-MnO NPs with high crystallinity and a high theoretical pseudocapacitance value within multilayers instead of OA-Fe_3O_4 NPs, the formed electrodes (i.e., $(CNT/OA\text{-}MnO\ NP)_{20}$ multilayers) exhibited a higher volumetric capacitance of $305 \pm 10\ F\ cm^{-3}$ ($183 \pm 5\ F\ g^{-1}$) (at a scan rate of $5\ mV\ s^{-1}$) than other conventional ultrathin supercapacitor electrodes, including manganese oxide or iron oxide NPs.

Introduction

The rapid expansion in the use of motor vehicles, various portable electronic devices and microscale systems has increased the demand for energy storage devices. Therefore, recent research efforts have been directed toward the fabrication of various high-performance batteries [1-5], fuel cells [6-8], and electrochemical capacitors [9-12]. Notably, electrochemical capacitors, which are also called supercapacitors, can provide higher power and exhibit longer lifespans but less energy than lithium-ion batteries and therefore have become important energy storage devices for high-power applications, such as the load leveling of heavy machinery, backup power supplies and integrated power supplies for on-chip micro-scale devices [13-20]. The performance of these electrochemical capacitors strongly depends on various processable properties, such as the active surface area of the electrode, the homogeneous electrode architecture, the internal resistance at the interfaces of active components, and the incorporation of active components into electrodes, as well as inherent properties, such as the specific capacitance and electric conductivity of the electrode materials. Therefore, the successful development of high-performance electrochemical capacitors is closely related to the realization of electrodes, enabling a high degree of control over electrode dimensions and highly uniform nano-architecture while simultaneously allowing the incorporation and controlled dispersion of a wide variety of electrochemical components.

Electrochemical capacitors are generally classified into two types according to their charge-storage mechanisms: (1) electric double-layer capacitors (EDLCs) with carbon electrodes [10,21-23] and (2) pseudocapacitors with high capacitive metal oxide electrodes [24-30]. Given that a theoretically high specific capacitance of transition metal oxides (TMOs) is obtained from nano-sized particles, the amount of charge stored in pseudocapacitors with TMO NPs is generally higher than that in conventional EDLCs [30]. Many characteristics, such as the size, crystallinity, crystal structure, and nanostructure shape, and the amount of adsorbed TMO NPs strongly affect the electrochemical behavior of supercapacitors [26,27,31]. Considering the characteristics of NPs, the synthesis of TMO NPs using hydrophobic ligands such as oleic acid (OA) in organic media is more desirable than TMO NP synthesis in aqueous media [32,33]. Additionally, when dispersed in organic media, these NPs should be highly stable without agglomeration, enabling the uniform adsorption of NPs and the resulting homogeneous film architecture during electrode preparation.

Recently, supercapacitor electrodes composed of conductive CNTs with an interconnected 3D porous network structure and TMO NPs with rapid surface redox reactions and high capacitance have been used to achieve both high energy and high power densities [34,35]. A critical design factor of CNT/TMO NP-based electrodes is the uniform incorporation of the high-energy TMO NPs into a CNT conducting matrix using simple and versatile techniques with a pore architecture and a high degree of control over the interface between the conducting matrix and the TMO NPs, which can enhance the electrochemical properties. With an optimized 3D nanocomposite structure, the void volume of the CNT matrix can be filled with numerous high-energy TMO NPs, which not only facilitate ionic and electronic transport to support the fast pseudocapacitive reactions of TMO NPs but also increase the volumetric energy density of the electrode. Additionally, long-term electrode stability is required for use in supercapacitors. Therefore, the stable and dense coating of active TMO NPs on the CNT matrix and its interfacial stability upon the charge/discharge cycling process should be considered important factors to improve the capacitance and cycling stability of composite electrodes with a limited volume. Jiang et al. reported that the volumetric capacitance ($1.26\ F \cdot cm^{-3}$ at a scan rate of $100\ mV\ s^{-1}$) of electrodes prepared from vertically aligned CNT forests with inserted nickel NPs was 5.7-fold greater than that of the pure CNT forest sample and that the supercapacitor also retained 94.2% of its initial capacitance after 10,000 cycles [28]. Although a vacuum-assisted electrodeposition method was partly employed to prepare the densely packed nickel NPs on the CNT forests for high-performance pseudocapacitor electrodes, a simplified solution manufacturing process is required to produce large-scale electrodes at low cost. Zhang et al. reported that CuO-CNT nanocomposite electrodes obtained through a solution blending process exhibited a specific capacitance ($62\ F \cdot g^{-1}$) that was 2.6-fold greater than that of a pure CNT electrode; further, this electrode retained approximately 83% of its initial capacitance after 1000 cycles [29].

Another promising approach is the electrostatic layer-by-layer (LbL) assembly method [31,36-43], which provides a simple route for the fabrication of a supercapacitor film with controlled thickness on the nanometer scale and with tailored composition by exploiting the electrostatic interactions between oppositely charged materials in aqueous media. In particular, for electrostatic LbL assembly, the inserted loading amount of TMO NPs, the film structure, and the electrochemical properties of nanostructured electrodes are strongly affected by various but complex assembly conditions, such as the pH, concentration, and/or ionic

strength of the deposition solution. Lee et al. recently reported that electrostatic LbL-assembled (charged CNT multilayers/amorphous MnO_x NP) electrodes displayed a high volumetric capacitance of 246 F cm^{-3} at 10 mV s^{-1}, showing the good operation stability (i.e., a decrease of 11.6% relative to the initial capacitance after 1000 cycles) [42]. More recently, Hyder et al. reported that an electrostatic LbL-assembled (cationic TiO_2 NP/anionic CNT)$_n$ film electrodes exhibited a maximum capacitance of 228 ± 19 F cm^{-3} at 1 mV s^{-1}, and excellent operation stability (i.e., a 7% loss in specific capacitance after 1000 cycles) [43]. These researchers used a cationic polyelectrolyte as a stabilizer for TiO_2 NPs to prevent NP agglomeration and achieve a high dispersion stability of NPs. However, these insulating polyelectrolytes, which were employed for electrostatic interaction between TiO_2 NPs and anionic CNTs, can increase the internal interfacial resistance within film electrodes.

To the best of our knowledge, most studies on supercapacitor electrodes using multilayer films have been based on electrostatic LbL assembly in aqueous media, and the resulting electrodes exhibited the low packing density of pseudocapacitive TMO NPs. Generally, the electrostatic repulsion among aqueous NPs with identical charges and the use of diluted NP concentration tend to limit the packing density of a NP layer to $<30\%$ [44,45]. Although it has been reported that the excessive loading of pseudocapacitive TMO NPs with low electrical conductivity onto CNTs can result in poor electrochemical performance, forming a dense but inhomogeneous electrode architecture [43], little experimental consensus exists on the TMO NP loading amount at which the electrochemical performance of supercapacitors is suppressed.

Here, we report on ultrathin supercapacitor electrodes based on direct covalent-bonding LbL-assembled (amine-functionalized CNT/oleic acid-stabilized TMO NPs)$_n$ (i.e., (CNT/OA-Fe_3O_4 NP)$_n$ and (CNT/OA-MnO NP)$_n$) multilayers formed in organic media instead of electrostatic LbL-assembly in aqueous media. The loading amount of highly stable TMO NPs in either toluene or hexane was manipulated using only the NP concentration without additional deposition conditions. The consecutive LbL-assembly of (CNT/OA-TMO NP)$_n$ multilayers was achieved by the direct formation of chemically stable covalent bonds between the CNTs and the metal oxide NPs, inducing the detachment of OA ligands from the surface of the TMO NPs. It should be noted that our approach requires no insulating polymer binder or polyelectrolyte stabilizer for high compatibility (or affinity) between the CNTs and TMO NPs and also has the advantage of minimizing the internal interfacial resistance of the electrodes due to the removal of insulating OA ligands during multilayer deposition.

Our study also focused on the preparation of ultrathin supercapacitor electrodes with a high loading amount of well-defined metal oxide NPs, a highly homogeneous electrode architecture, a high capacitance in a limited volume, a good rate capability, and a high long-term cycling stability, which can be effectively applied to microscale energy-storage devices [46] such as nanorobotics, microelectromechanical systems, and wearable personal electronics. Additionally, we investigated the relationships among the loading amount of OA-TMO NPs, the film conductivity, and the volumetric capacitance of the film electrode, which can provide a basis for optimizing and enhancing the performance of ultrathin film-type supercapacitors. It should be noted that the 8 nm-sized OA-Fe_3O_4 NPs and 11 nm-sized MnO NPs used in our system were selected as inexpensive, non-toxic, and well-defined pseudocapacitive NPs in contrast to expensive RuO_2 [47] and amorphous MnO_2 NPs [42,48]. Although it has been reported that conventional Fe_3O_4 NPs synthesized in aqueous solution exhibit a low specific capacitance (<40 F g^{-1}) [49], the specific capacitance of well-defined OA-Fe_3O_4 NPs synthesized in nonpolar media was measured to be approximately 75 F g^{-1} (the measurement details will be shown in the Supporting Information, Experimental Details). Additionally, the (CNT/OA-Fe_3O_4 NP)$_n$ electrodes prepared using our approach can exhibit high volumetric capacitance (approximately 248 ± 15 F cm^{-3} at 5 mV s^{-1}), excellent cycling stability (99.2% of the initial capacitance after 1000 cycles), and good rate capability, allowing a OA-Fe_3O_4 NP loading of 78%. In particular, this volumetric capacitance was significantly higher (more than three-fold) than that of conventional supercapacitor electrodes composed of carbon-based materials and iron oxide NPs. Furthermore, when employing OA-MnO NPs with intrinsically high pseudocapacitance values instead of OA-Fe_3O_4 NPs, the volumetric capacitance of the (CNT/OA-MnO NP)$_n$ electrodes could be increased up to 305 ± 10 F $\cdot$ cm^{-3} (at 5 mV s^{-1}), which is superior to that of other conventional (manganese oxide-based) supercapacitor electrodes. Considering that the performance of supercapacitors strongly depends on the loading amount of NPs, the qualities of NPs, the conductivity, and the type of interfacial bonding between the conductive materials and the pseudocapacitive NPs, our approach can provide a basis for significantly enhancing the electrochemical performance of supercapacitor electrodes.

Experimental section

The functionalization of CNTs (i.e., amine- or carboxylic acid-functionalized CNTs) and oleic-acid-stabilized transition metal oxide nanoparticles (i.e., OA-Fe_3O_4, OA-MnO, and OA-TiO_2) was established using a previously reported protocol. The experimental details are provided in the Supporting Information.

Results and discussion

Ultrathin LbL-assembled (CNT/OA-TMO NP)$_n$ multilayers for supercapacitor film electrodes were prepared through LbL assembly in organic media. First, the OA-Fe_3O_4 NPs, which were prepared in toluene and had diameters of approximately 8 ± 1 nm (Fig. 1**a**), were directly deposited onto substrates coated with CNTs. In this case, the OA ligands, which are loosely bound to the surfaces of the Fe_3O_4 NPs, can be replaced by the CNTs through a ligand exchange reaction due to the high affinity between the Fe_3O_4 NPs and the NH_2 groups of the CNTs [41]. Although the carboxylate ion (COO^-) group acts as either a chelating ligand that binds to Fe through two O atoms or as a monodentate ligand that links to Fe through only one O atom [32], the carboxylate-based ligands around each Fe_3O_4 NP can be replaced by surfactants containing a functional group with a high affinity

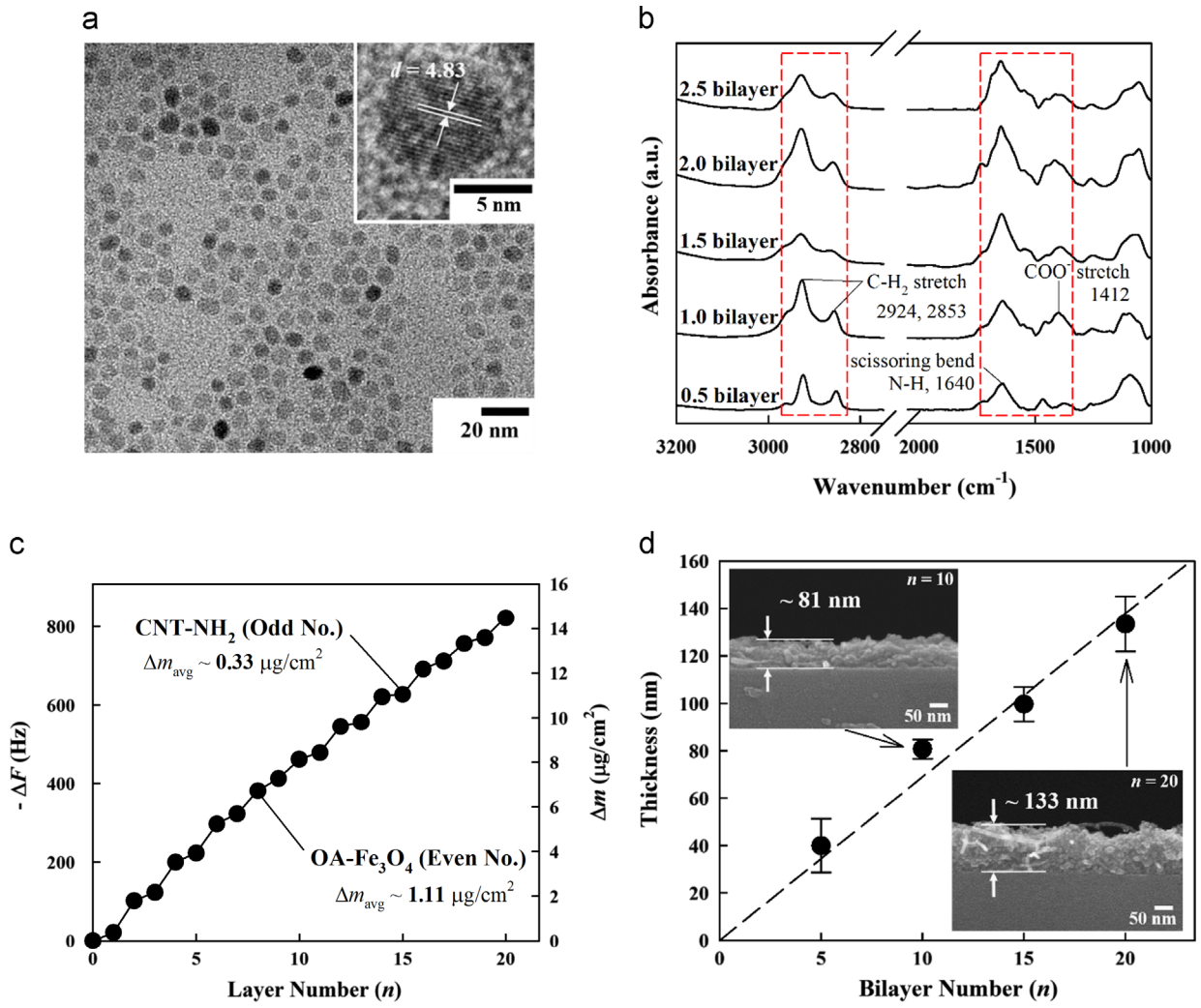

Fig. 1 (a) HR-TEM image of the approximately 8±1 nm OA-Fe_3O_4 NPs. (b) FTIR spectra of the (CNT/OA-Fe_3O_4 NP)$_n$ multilayers. (c) Frequency and mass change of the (CNT/OA-Fe_3O_4 NP)$_n$ multilayers as a function of the layer number (n). (d) Total film thicknesses of the (CNT/OA-Fe_3O_4 NP)$_{n=5,\ 10,\ 15,\ \text{and}\ 20}$ multilayers measured from the cross-sectional SEM images.

for Fe. This ligand exchange between the OA ligands bound to the Fe_3O_4 NPs and the NH_2 groups of the CNTs was verified by Fourier-transform infrared spectroscopy (FTIR), as illustrated in Fig. 1**b**. The C-H stretching (2924 and 2853 cm^{-1}) and COO^- stretching (1601, 1530, and 1412 cm^{-1}) peaks originated from the long aliphatic chains and carboxylate (COO^-) groups of the OA ligands bound to the Fe_3O_4 NPs. It has been reported that the COO^- stretching (i.e., asymmetric $\nu_{as}(COO^-)$ and symmetric $\nu_s(COO^-)$) peaks appear in place of the $C{=}O$ stretching (1710 cm^{-1}) peak from the carboxylic acid (COOH) group when OA ligands are adsorbed onto the surface of Fe_3O_4 NPs [50,51]. The N-H bending and C-N bond stretching vibrations at 1640 and 1120 cm^{-1}, respectively, are attributed to the amine-functionalized CNTs [52,53]. Notably, the COO^- stretching peaks at 1601 and 1530 cm^{-1} arising from the OA-Fe_3O_4 NPs nearly overlapped with the N-H bending mode of the CNT (Fig. S1 in Supporting Information). Therefore, the two adsorption peaks at 1640 and 1412 cm^{-1} were attributed to the N-H bending of the CNT and to the COO^- stretching of the OA ligand embedded within the LbL-assembled CNT/OA-Fe_3O_4 NP film.

Following the subsequent adsorption of the OA-Fe_3O_4 layer onto the CNT-coated film (i.e., OA-Fe_3O_4 NP/CNT/substrate), the adsorption peaks for C-H stretching (2924 and 2853 cm^{-1}) and COO^- stretching (1412 cm^{-1}), which arise from the loosely bound OA ligands mentioned above, significantly increased after the deposition of the OA-Fe_3O_4 layer. These characteristic peaks decreased again when the CNT layer was subsequently deposited onto the outermost OA-Fe_3O_4 layer, which resulted from the replacement of OA ligands by the amine moieties of the CNTs. Although weak C-H and COO^- stretching peaks of the OA ligands were still observed due to the presence of the partially unbound sites between the OA-Fe_3O_4 NPs and CNTs because of the porous structure of the CNT layer, the decrease in the intensities of the C-H and COO^- stretching peaks implies that a large quantity of OA ligands bound to the outermost surface of the Fe_3O_4 NPs was substituted with the CNTs when the outermost layer was changed from OA-Fe_3O_4 to a CNT layer. Conversely, when the outermost layer was then changed from CNTs to OA-Fe_3O_4 NPs, the C-H and COO^- stretching peaks (2924, 2853, and 1412 cm^{-1}) of the OA ligand increased again. As the CNT layer was further adsorbed onto the outermost OA-Fe_3O_4 NP-coated

film as a function of deposition time, the absorption peak intensity of the COO^- stretching at 1412 cm^{-1} significantly decreased at 20 min and reached a plateau after 30 min (Fig. S2 in Supporting Information). Although the COO^- stretching peak of OA ligands at 1412 cm^{-1} were still observed even after sufficient adsorption time, these phenomena are mainly due to the presence of unbounded sites between porous CNT chains and OA-Fe_3O_4 NPs. However, a notable decrease in peak intensity of OA ligand absorbance indicates that the formation of (CNT/OA-Fe_3O_4 NP)$_n$ multilayer films can be induced by the ligand-exchange reaction between the OA ligands of the Fe_3O_4 NPs and the NH_2 groups of the CNTs instead of conventional electrostatic LbL assembly, yielding a low packing density of Fe_3O_4 NPs (Scheme 1). It should also be noted that various hydrophobic OA-TMO NPs, which include either OA-MnO or OA-TiO_2 and OA-Fe_3O_4 NPs, can be LbL-assembled with CNTs (Fig. S3 in Supporting Information).

The loading amounts of CNTs and OA-Fe_3O_4 NPs embedded within the multilayers were quantified by quartz crystal microscopy (QCM) (Fig. 1**c**). In this case, the concentrations of the CNT and OA-Fe_3O_4 NP solutions used for LbL assembly were 2 and 10 mg · mL^{-1}, respectively. Measuring the frequency changes (ΔF) from which the mass changes (Δm) were calculated for the alternating deposition of CNT and OA-Fe_3O_4 NP yielded $-\Delta F$ values of 19 ± 3 Hz (Δm of approximately 330 ng · cm^{-2}) and 63 ± 11 Hz (Δm of approximately 1110 ng · cm^{-2}), respectively. The formation of (CNT/OA-Fe_3O_4 NP)$_n$ multilayers was further characterized using field-emission scanning electron microscopy (FE-SEM) (Fig. 1**d**). The total thickness of each (CNT/OA-Fe_3O_4 NP)$_n$ multilayer film was investigated as a function of the number of bilayers and then was measured at approximately 40 nm for $n=5$, 81 nm for $n=10$, 100 nm for $n=15$, and 133 nm for $n=20$.

Based on the adsorbed quantities and film thicknesses of the (CNT/OA-Fe_3O_4 NP)$_n$ multilayers, the mass density of the multilayers was calculated to be approximately 1.94 ± 0.02 g · cm^{-3} (the density of Fe_3O_4 is 5.0 g cm^{-3}). The high packing density of the OA-Fe_3O_4 NPs onto CNT was visually confirmed using high-resolution transmission electron microscopy (HR-TEM) (Fig. 2**a**). It should be noted that such a high density of (CNT/OA-Fe_3O_4 NP)$_n$ films prepared from covalent-bonding LbL-assembly (more specifically, ligand-exchange LbL-assembly) in organic media has not been readily achieved through traditional electrostatic LbL-assembly (Fig. S4 in Supporting Information). To further clarify these issues, water-dispersible pentacyclooctasiloxane octakis hydrate-octakis (tetramethylammonium)-stabilized Fe_3O_4 NPs (i.e., octakis-Fe_3O_4) were prepared by stabilizer exchange from oleic acid to the negatively charged octakis, and then, octakis-Fe_3O_4 NPs were electrostatically adsorbed onto positively charged CNTs. Here, the formed NP array exhibited a level of decorated adsorption (i.e., a low packing density) due to the long-range electrostatic repulsion between identically charged NPs despite the same deposition conditions (i.e., NP concentration of approximately 10 mg mL^{-1}) as those used for the adsorption of OA-Fe_3O_4 NPs (Fig. 2**b**). Additionally, the mass density of the (cationic CNT/anionic octakis-Fe_3O_4 NP)$_n$ multilayers was calculated to be approximately 1.2 g · cm^{-3}. The density of electrostatic LbL-assembled (anionic CNT/cationic TiO_2)$_n$ films was recently reported to be 0.86 ± 0.06 g · cm^{-3} (the density of TiO_2 is approximately 3.84 g · cm^{-3}) [43]. These results suggest the possibility that direct covalent-bonded LbL-assembled films with densely packed OA-Fe_3O_4 NPs can be effectively used to enhance the pseudocapacitive performance of the porous CNT-based electrode within a defined volume.

The dense packing of OA-Fe_3O_4 NPs was also confirmed by the surface wettability determined using water contact angle measurements. Surface wettability measurements, which are known to be quite sensitive to the chemical and physical properties of the uppermost surface in the range of a few nanometers (nm), are strongly affected by the chemical structure and physical interdigitation present in sequentially adsorbed components [54,55]. In this case, the alternating LbL deposition of CNTs and OA-Fe_3O_4 NPs leads to a highly periodic alternation in the water contact angle

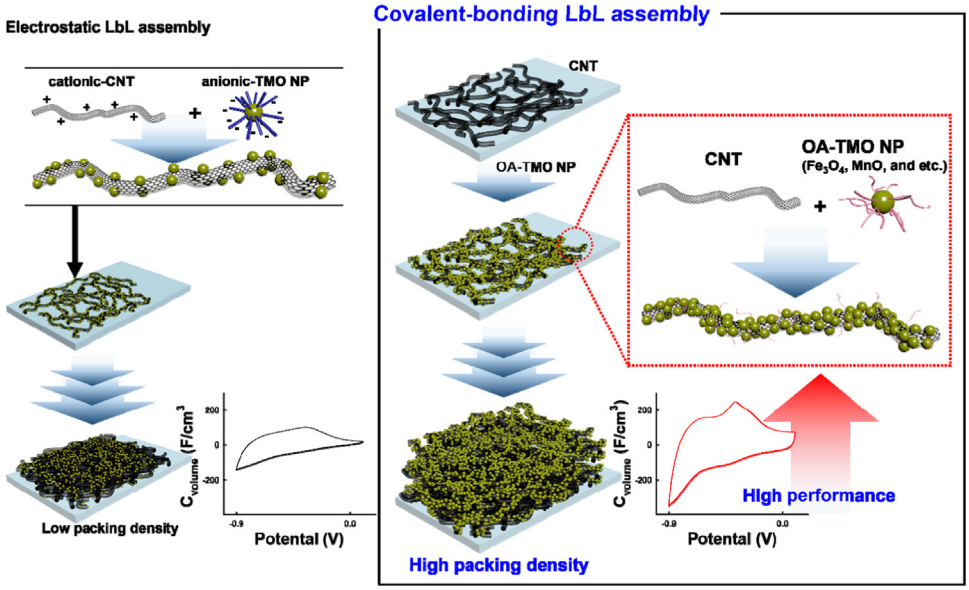

Scheme 1 Schematic of the (CNT/OA-TMO NP)$_n$ multilayer using direct covalent-bonding LbL assembly.

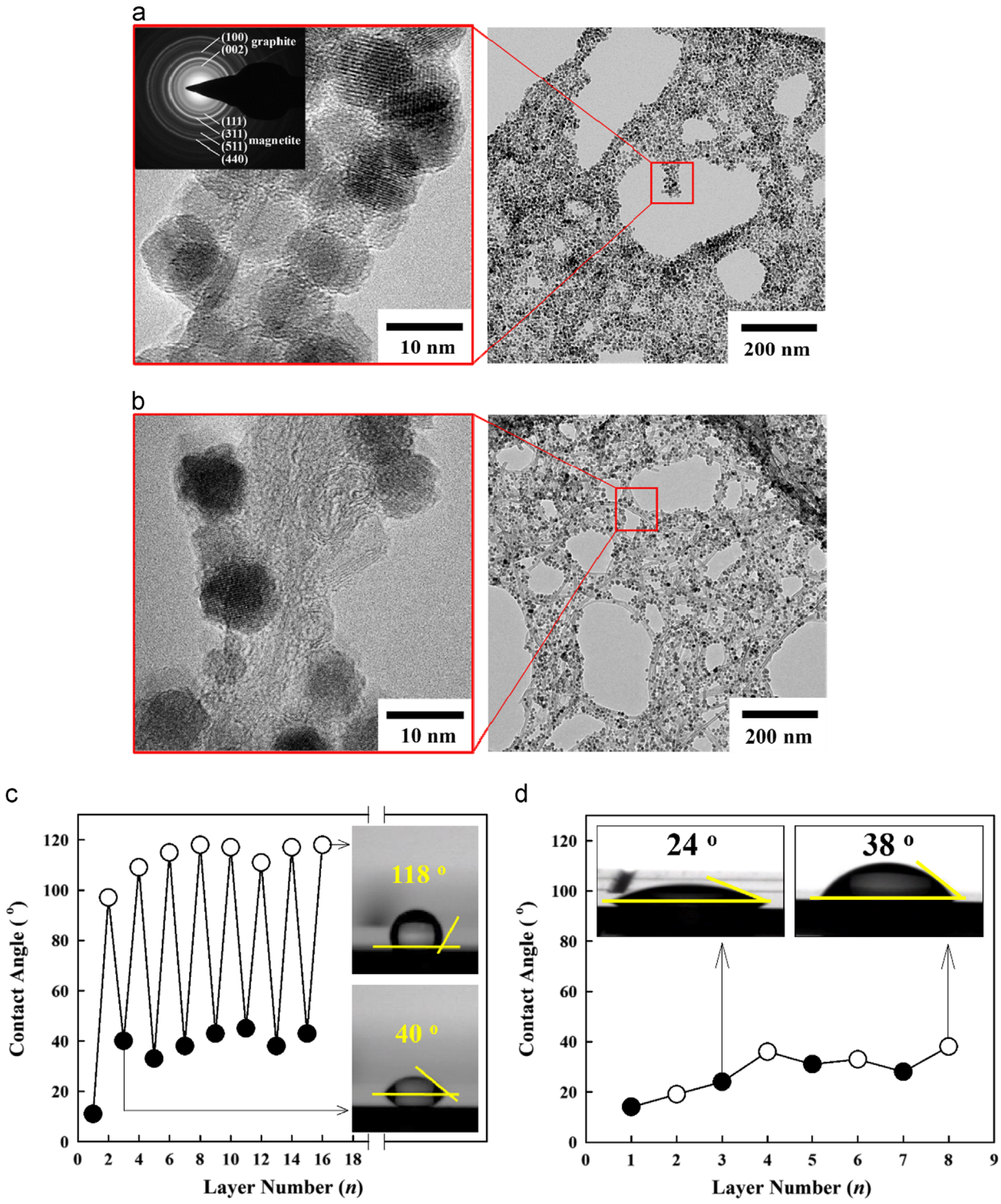

Fig. 2 HR-TEM images of (a) CNT/OA-Fe_3O_4 NPs and (b) cationic CNT/anionic octakis-Fe_3O_4 NPs. Anionic octakis-Fe_3O_4 NPs in water were prepared by stabilizer exchange from oleic acid to the negatively charged octakis. The inset presents the SAED pattern of CNT/OA-Fe_3O_4 NPs. Water contact angles measured from (c) the (2 mg · mL^{-1} CNT/10 mg · mL^{-1} OA-Fe_3O_4 NP)$_n$ and (d) the (2 mg mL^{-1} CNT/1 mg mL^{-1} OA-Fe_3O_4 NP)$_n$ multilayers. Odd and even numbers indicate the layers deposited with CNTs and OA-Fe_3O_4 NPs, respectively.

on the resulting multilayer films between approximately $30 \pm 9^\circ$ and $113 \pm 5^\circ$ (Fig. 2**c**). These phenomena imply that the densely packed OA-Fe_3O_4 NP layer significantly lowers the degree of interdigitation between the preadsorbed and subsequently adsorbed CNT layers that occurs during the LbL growth of multilayer films, in addition to effectively screening the chemical properties of CNT. However, if the OA-Fe_3O_4 NPs are loosely packed on the CNTs, no apparent

oscillation in the water contact angle is observed (Fig. 2**d**), implying that the surface wettability of the outermost layer strongly reflects the chemical and physical properties of the CNTs and OA-Fe_3O_4 NPs [55]. That is, these results indicate that the hydrophobic and hydrophilic properties of the film surface can be dramatically changed by the dense packing of OA-Fe_3O_4 NPs.

The quality of the OA-Fe_3O_4 NPs used in our study was investigated with respect to their magnetic properties. For this purpose, the magnetic characterization of (CNT/OA-Fe_3O_4 NP)$_n$ films as a function of the number of bilayers was performed using a superconducting quantum interference device (SQUID) magnetometer in the field range from -4000 to $+4000$ Oe. The magnetization curves of these nanocomposites were measured at room temperature ($T=300\ K$) and found to be reversible without coercivity, remanence, or hysteresis, suggesting typical superparamagnetic behavior (Fig. 3**a**). The saturated magnetization increased regularly with increasing bilayer number and with the total amount of OA-Fe_3O_4 NPs adsorbed within the multilayer films. The magnetization per gram of adsorbed OA-Fe_3O_4 NPs was similar for different multilayered films, and a high saturated magnetism of approximately 150 emu g^{-1} was observed with negligible differences (Fig. 3**b**). Mamedov et al. reported that the saturated magnetism of LbL multilayer films based on electrostatically charged Fe_3O_4 NPs is approximately 4.00×10^{-3} emu g^{-1} at 10 *K* [56]. However, at liquid helium temperature ($T=5\ K$), the thermally activated magnetization flipping properties of the (CNT/OA-Fe_3O_4 NP)$_n$ nanocomposites exhibited frustrated superparamagnetic behavior (Fig. 3**c**). That is, the magnetization curves acquired a loop shape with distinct separation between the two sweeping directions, which is typically observed for ferromagnets. Fig. 3**d** shows the temperature dependence of the magnetization of the nanocomposites from 300 *K* to 5 *K* under an applied magnetic field of 150 Oe. The blocking temperature (T_B), which began to deviate between the zero-field-cooling (ZFC) and field-cooling (FC) magnetization states, was fixed at approximately 61 *K*. Park et al. reported that pristine OA-Fe_3O_4 NPs with diameters of approximately 8 nm exhibit a T_B of 61 *K* [33]. These results clearly demonstrate that the (CNT/OA-Fe_3O_4 NP)$_n$ nanocomposite multilayers retained the inherent properties of Fe_3O_4 NPs and that the synthesis of OA-Fe_3O_4 NPs in

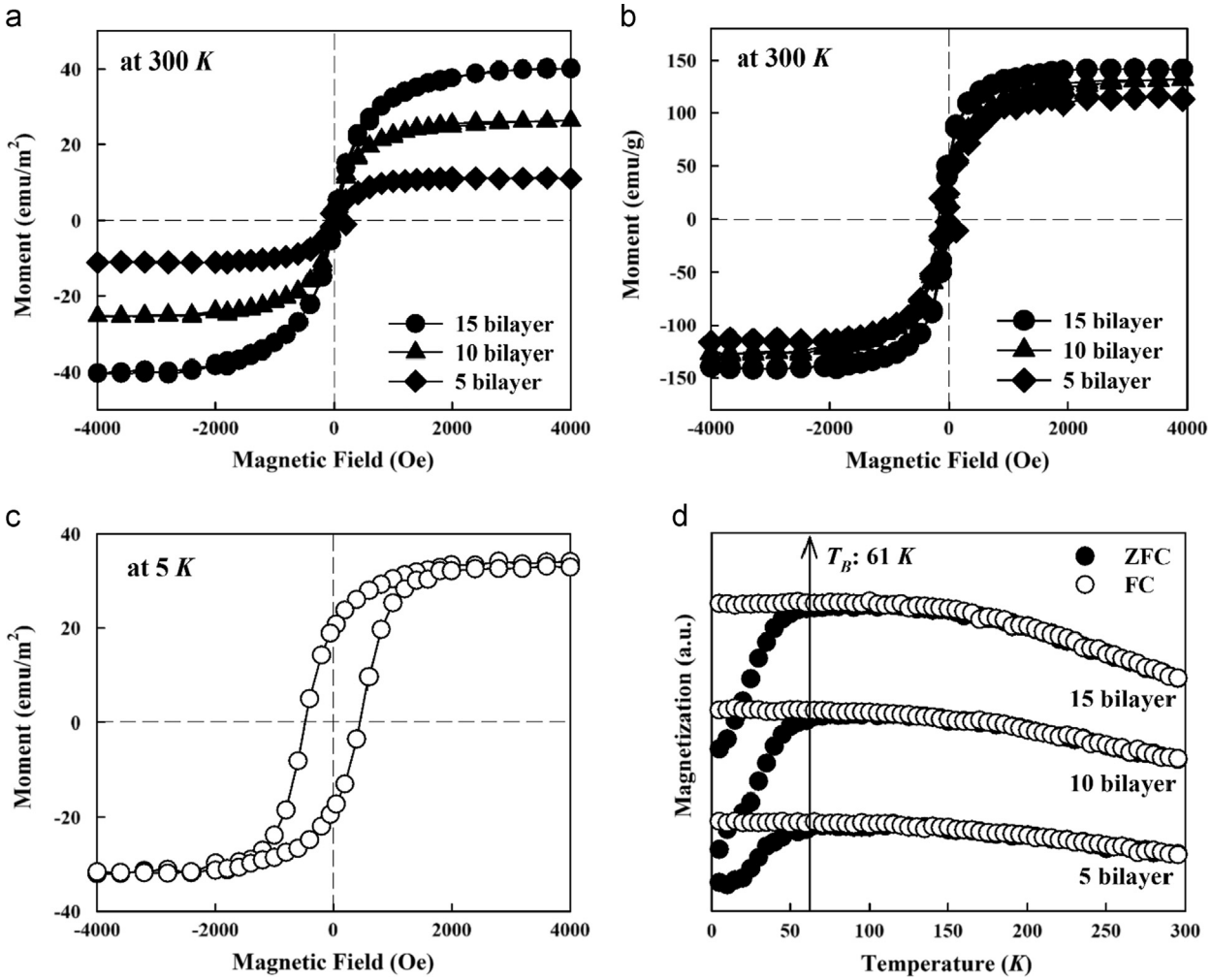

Fig. 3 (a) The magnetization curves of (CNT/OA-Fe_3O_4 NP)$_{n=5,\ 10,\ \text{and}\ 15}$ multilayer films measured at 300 K. (b) The magnetization curves of (CNT/OA-Fe_3O_4 NP)$_{n=5,\ 10,\ \text{and}\ 15}$ multilayer films divided by the mass of adsorbed OA-Fe_3O_4 NPs within multilayers. (c) The magnetization curve of (CNT/OA-Fe_3O_4 NP)$_{10}$ multilayer films at 5 K. (d) Temperature dependence of zero-field-cooling (ZFC) and field-cooling (FC) magnetization measured using 150 Oe.

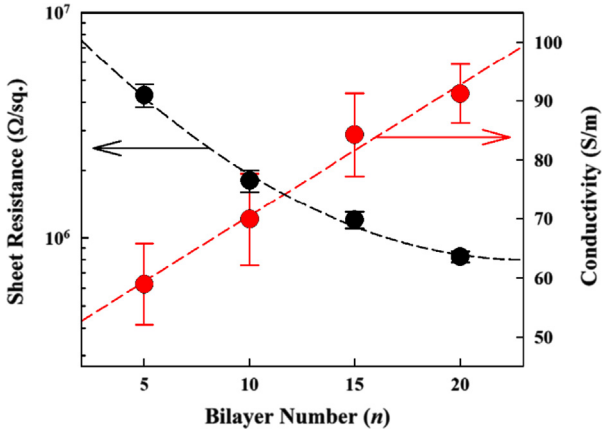

Fig. 4 Electrical conductivity of (CNT/OA-Fe_3O_4 NP)$_{n=5,\ 10,\ 15,\ and\ 20}$ multilayer films as a function of the bilayer number (*n*).

nonpolar media yielded superior characteristics (e.g., crystallinity, size distribution, and magnetic properties) to those of electrostatically charged Fe_3O_4 NPs synthesized in aqueous media. Additionally, the blocking temperature of Fe_3O_4 NP array has also been reported to shift to significantly higher temperatures when the isolated array was changed into a 3D NP array because of the relatively strong dipole interactions between the magnetic moments of the individual particles [57]. However, the fixed blocking temperature shown in our study suggest that the CNT/OA-Fe_3O_4 NP multilayers could preserve the intrinsic magnetic properties of the isolated NPs because the interposed CNT layers separate the NPs and, thus, effectively block the dipole interactions between the magnetic Fe_3O_4 NPs.

The electrical properties of the (CNT/OA-Fe_3O_4 NP)$_n$ multilayers were investigated by measuring the sheet resistance of the multilayered films using a four-point probe, as shown in Fig. 4. The sheet resistance and conductivity of the (CNT/OA-Fe_3O_4 NP)$_n$ multilayers decreased from 4.3×10^6 to 8.2×10^5 $\Omega \cdot \square^{-1}$ and increased from 60 to 92 S m^{-1} as the bilayer number (*n*) increased from 5 to 20 (i.e., the film thickness increased from 40 to 133 nm), respectively. It has recently been reported that the conductivity of electrostatic LbL-assembled (cationic TiO_2 NP/anionic CNT)$_n$ multilayers was significantly increased with increasing bilayer number (*n*) due to the increased percolation of CNTs. However, for LbL-assembled multilayers composed of poly(ethylene imine) (PEI) and OA-Fe_3O_4 NPs, these films could not be measured using the four-point probe method due to their extremely high resistance ($> \sim 10^8\ \Omega \cdot \square^{-1}$). Although Fe_3O_4 has been reported to possess high electrical conductivity ($\sim 2 \times 10^4\ S \cdot m^{-1}$) [58], the reduced diameter of the Fe_3O_4 NPs increases the resistivity due to nanosize effects related to the increased surface-to-volume ratio [59]. These results clearly indicate that the CNTs can operate as continuous conductive pathways within the (CNT/OA-Fe_3O_4 NP)$_n$ multilayer, inducing the removal of insulating OA ligands bound to the surface of Fe_3O_4 NPs during multilayer fabrication even though the densely packed Fe_3O_4 NP arrays lower the level of interdigitation between neighboring CNT layers. To more evidently confirm these phenomena, electrochemical impedance spectroscopy (EIS) measurements of 133 nm-thick (CNT/OA-Fe_3O_4 NP) and the 131 nm-thick (PEI/OA-Fe_3O_4 NP) multilayer electrodes were conducted in the frequency range from 1 MHz to 0.1 Hz at potential amplitude of 10 mV (Fig. S5 in Supporting Information). In this case, the equivalent-series resistance of the 133 nm-thick (CNT/OA-Fe_3O_4 NP) and the 131 nm-thick (PEI/OA-Fe_3O_4 NP) multilayer films were measured to be 67.5 and 90.5 Ω, respectively. These results evidently demonstrate that porous (CNT/OA-Fe_3O_4 NP)$_n$ multilayers are effective for facilitating ion and electron transfer compared to the OA-Fe_3O_4 NP-based multilayers containing insulating polymers.

Based on these results, we explored the possibility that the (CNT/OA-Fe_3O_4 NP)$_n$ multilayers could be effectively used as an utrathin supercapacitor electrode. For this investigation, the electrochemical performance of (CNT/OA-Fe_3O_4 NP)$_n$ multilayers deposited on an indium tin oxide (ITO) substrate was evaluated using cyclic voltammetry (CV) and galvanostatic charge/discharge measurements. The cell included a Pt mesh as the counter electrode and Ag/AgCl reference electrode in a 0.1 M Na_2SO_3 electrolyte rather than a harsh acidic electrolyte. First, CV was employed to examine the charge-storage capacities of the (CNT/OA-Fe_3O_4 NP)$_n$ multilayer electrodes. Here, the CV scans were performed in the potential window between −0.9 V and +0.1 V to prevent degradation of the (CNT/OA-Fe_3O_4 NP)$_n$ multilayer electrodes and electrolyte at higher potentials. Fig. 5**a** presents the CV data for the (CNT/OA-Fe_3O_4 NP)$_{n=5\text{-}20}$ electrodes at a scan rate of 5 mV s^{-1} as a function of the bilayer number (*n*). The current level of the asymmetric CV curve with a redox peak was observed to increase with increasing bilayer number (or total film thickness) of the multilayer electrode. Furthermore, the total integrated charge density (in mC · cm^{-2}) was calculated using the integrated area of the CV curves shown in Fig. 5**a**. In this case, the total charge density of the (CNT/OA-Fe_3O_4 NP)$_n$ electrodes increased almost linearly with the bilayer number of the multilayer electrodes, implying that the total electrode capacity can be further enhanced and precisely adjusted by adjusting the bilayer number (Fig. 5**b**). In contrast, the CV curve of the hydrogen-bonded LbL-assembled (amine-functionalized CNT/carboxylic acid-functionalized CNT)$_n$ (i.e., H-bonded (CNT/CNT)$_n$) electrode, which corresponds to the (CNT/OA-Fe_3O_4 NP)$_n$ electrode, exhibited a rectangular shape with a relatively low current level in the potential range of −0.9 to +0.1 V, which is characteristic of double layer capacitance (*a more detailed explanation is given in a later section*). Based on these results, it is reasonable to conclude that the lack of symmetry in the CV curve with a redox peak from the (CNT/OA-Fe_3O_4 NP)$_n$ electrodes was mainly due to the contribution of the pseudocapacitive Fe_3O_4 NPs to the total capacitance. In this case, the total capacity of the (CNT/OA-Fe_3O_4 NP)$_{20}$ electrode was approximately 3.8-fold higher than that of the H-bonded (CNT/CNT)$_{20}$ electrode thermally treated at 150 °C (Fig. S6 in Supporting Information).

The (CNT/10 mg mL^{-1} OA-Fe_3O_4 NP)$_{20}$ electrodes also exhibited good pseudocapacitive behavior as the scan rate increased from 5 to 400 mV s^{-1}, suggesting that the multilayer electrodes possess properties of rapid charge transfer and cation diffusion and, consequently, good rate capability despite the densely packed OA-Fe_3O_4 NP layers (Fig. 5**c**). However, a further increase in the scan rate caused a shift in the peak current toward higher potentials during the charging step due to poor reaction kinetics [42,60]. Although the capacitance values decreased as the scan rate increased, which is normal behavior for electrochemical charge storage

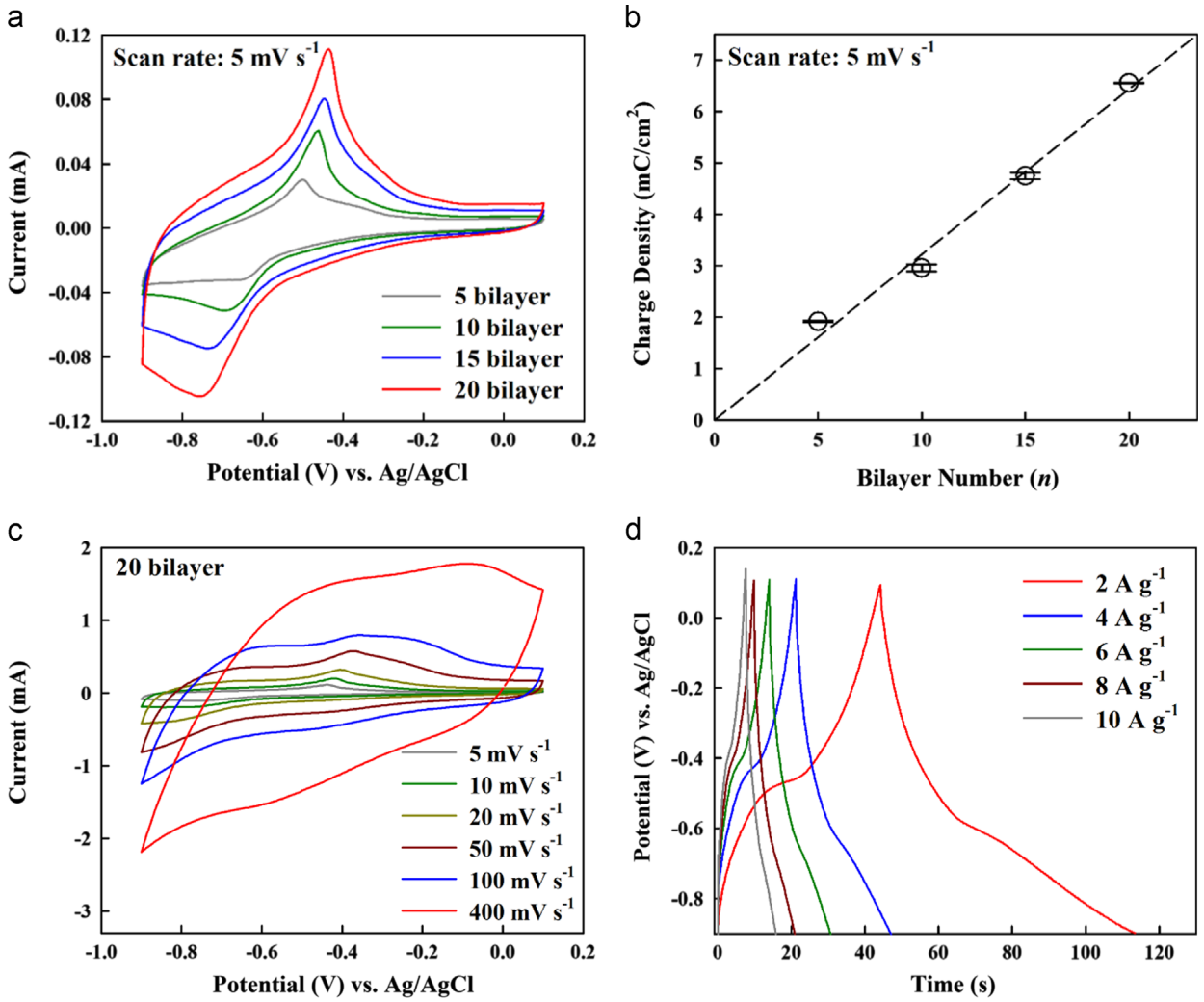

Fig. 5 (a) Cyclic voltammograms of LbL-assembled $(CNT/OA\text{-}Fe_3O_4\ NP)_{n=5,\ 10,\ 15,\ and\ 20}$ electrodes at a scan rate of 5 mV s^{-1}. (b) Total integrated charge of the LbL-assembled $(CNT/OA\text{-}Fe_3O_4\ NP)_n$ electrodes at a scan rate of 5 mV s^{-1} as a function of the bilayer number (*n*). (c) Cyclic voltammograms of the LbL-assembled $(CNT/OA\text{-}Fe_3O_4\ NP)_{20}$ electrode as a function of the scan rate (5 to 400 mV s^{-1}). (d) Galvanostatic charge-discharge curves of $(CNT/OA\text{-}Fe_3O_4\ NP)_{20}$ electrodes at different current densities ranging from 2 to 10 A g^{-1}.

systems (Fig. S7a in Supporting Information), the $(CNT/OA\text{-}Fe_3O_4\ NP)_n$ multilayer electrode prepared from OA-Fe_3O_4 NP solution with relatively low concentration (i.e., 0.1 mg mL^{-1} OA-Fe_3O_4 NP) can decrease the decay rate of capacitance by an increase of scan rate (Fig. S7b in Supporting Information). That is, at high scan rates, protons or alkaline metal cations reached the outer surface layer of the electrode, and the interior pores of the OA-Fe_3O_4 NPs had significant difficulty in being utilized. Another possibility may be attributed to the surface adsorption process [61] at higher scan rates. Accordingly, a portion of the surface of the electrode materials contributed a high charging/discharging rate, which decreased the specific capacitance [62].

Fig. 5**d** shows the changes in the galvanostatic charge-discharge curves of the $(CNT/OA\text{-}Fe_3O_4\ NP)_{20}$ film electrodes as the current density was increased from 2 to 10 $A \cdot g^{-1}$. As shown in Fig. 5**d**, the inclined parts (or minor charge-discharge plateau) in the charging potential window in the range from −0.5 to −0.4 V and the discharging potential window in the range from −0.6 to −0.7 V indicate superimposed redox reactions, which correspond to the redox peak of the CV curves in Fig. 5**a**. More specifically, at values greater than −0.4 V, the time dependence of the potential is linear, implying pure double-layer capacitance behavior from the charge separation at the electrode-electrolyte interface. In contrast, at values less than −0.4 V, the time dependence of the potential is nonlinear due to the typical pseudocapacitance behavior of OA-Fe_3O_4 as an inserted electrode material. These phenomena are in stark contrast with the linear time-dependent behavior of the H-bonded $(CNT/CNT)_n$ electrodes without OA-Fe_3O_4 NPs (Fig. S8 in Supporting Information). It has been reported that the redox behavior of solution blending-based nanocomposite electrodes composed of Fe_3O_4 nanosheets and carbon nanofibers is mainly due to reversible multielectron redox reactions (i.e., surface redox reactions of sulfur in the form of sulfate and sulfite anions and the redox reactions between Fe^{II} and Fe^{III}) of the inserted Fe_3O_4 NPs in an electrolyte solution [61,63].

Considering that the $(CNT/OA\text{-}Fe_3O_4\ NP)_n$ film electrodes with an extremely high density of approximately 1.94 $g \cdot cm^{-3}$

exhibit double-layer capacitance and pseudocapacitance behaviors, it is reasonable to hypothesize that these electrodes prepared from covalent-bonding LbL-assembly are superior to the traditional nanocomposite (i.e., solution-blended [29,61,63], vacuum-deposited [28], and electrostatic LbL-assembled nanocomposites [42]) electrodes composed of CNTs and/or Fe_3O_4 NPs with respect to the volumetric capacitance. To confirm these possibilities, we prepared electrostatic LbL-assembled (cationic CNT/anionic octakis-Fe_3O_4 NP) and H-bonded (CNT/CNT) film electrodes with partial amide bonds after thermal treatment at 150 °C (Fig. 6a). Notably, for the electrostatic LbL (cationic CNT/anionic octakis-Fe_3O_4 NP) film, the 10 mg · mL^{-1} OA-Fe_3O_4 NPs were phase-transferred from toluene to aqueous media using anionic octakis ligands, and the resulting 10 mg · mL^{-1} anionic octakis-Fe_3O_4 NPs were LbL-assembled with the cationic CNT layer. The number of bilayers in the above-mentioned films was determined to be similar to the total film thickness of 40 nm of the (CNT/OA-Fe_3O_4 NP) electrodes. In these cases, the current and area in the CV curve for the 40-nm-thick (CNT/OA-Fe_3O_4 NP) film electrodes were significantly larger than those for the 55-nm-thick H-bonded (CNT/CNT) and the 45-nm-thick (cationic CNT/anionic octakis-Fe_3O_4 NP) electrodes at a scan rate of 50 mV s^{-1} and with the same electrolyte solution. These results indicate that the (CNT/OA-Fe_3O_4 NP)$_n$ film electrode with a densely packed OA-Fe_3O_4 array can effectively utilize the high energy density of Fe_3O_4 NPs with multielectron redox reactions for electrochemical capacitor applications. To further investigate these possibilities, the volumetric capacitances of the (CNT/OA-Fe_3O_4 NP)$_{20}$ film electrodes were calculated from the CV curves for a quantitative comparison with those of the (cationic CNT/anionic octakis-Fe_3O_4 NP)$_{20}$ and H-bonded (CNT/CNT)$_{20}$ electrodes (**Experimental Details in** Supporting Information). The (CNT/OA-Fe_3O_4 NP)$_{20}$, (cationic CNT/anionic octakis-Fe_3O_4 NP)$_{20}$, and H-bonded (CNT/CNT)$_{20}$ electrodes exhibited maximum volumetric capacitances of approximately 248, 141, and

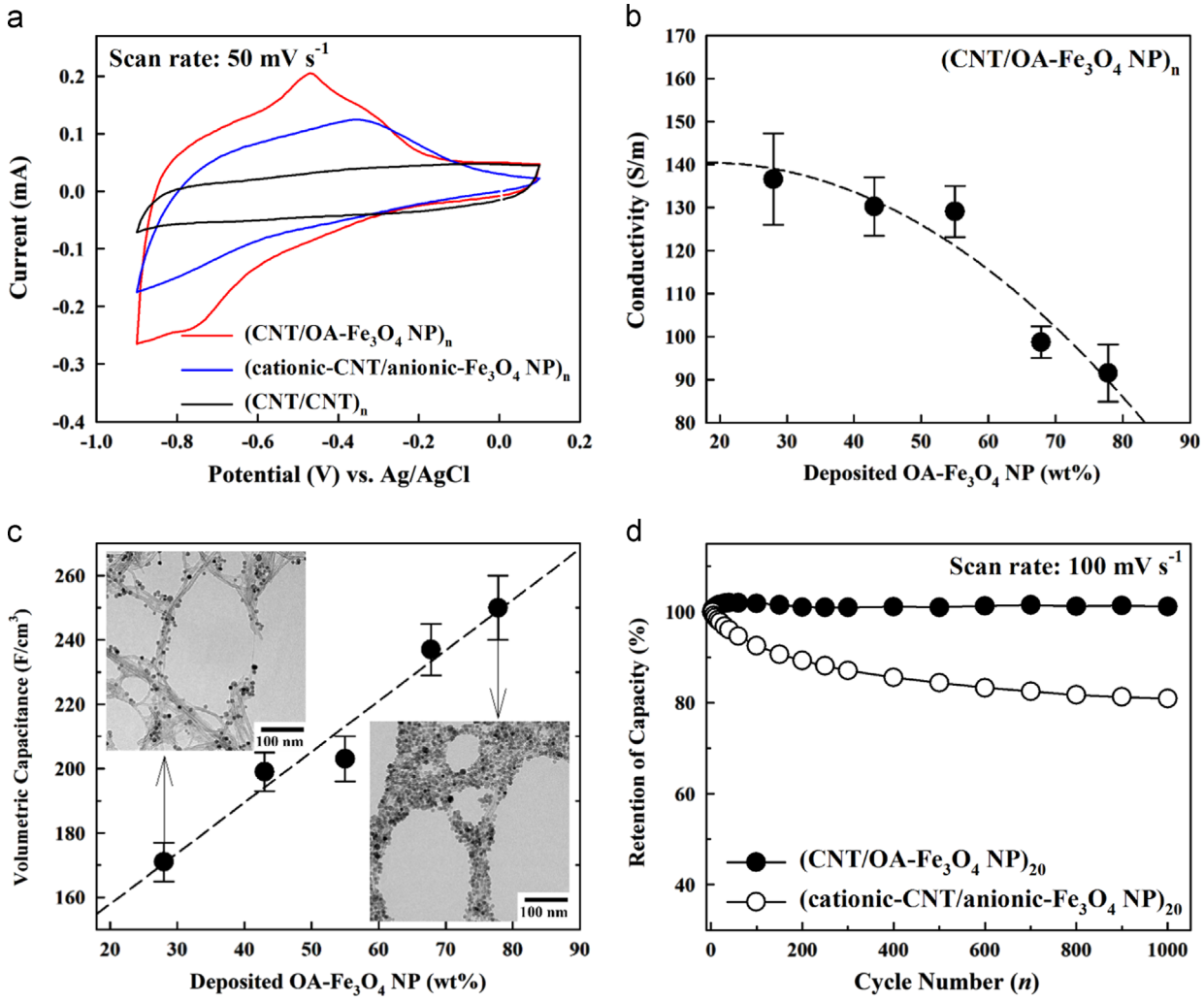

Fig. 6 (a) Cyclic voltammograms of 45-nm-thick (cationic CNT/anionic octakis-Fe_3O_4 NP), 55-nm-thick H-bonded (CNT/CNT) and 40-nm-thick (CNT/OA-Fe_3O_4 NP) electrode films at a scan rate of 50 mV s^{-1}. (b) Conductivities of the (CNT/OA-Fe_3O_4 NP)$_n$ multilayer electrodes as a function of the OA-Fe_3O_4 NP loading. In this case, loading amounts of 28, 42, 54, 68, and 78 wt % OA-Fe_3O_4 NPs within films were obtained from 0.1, 0.5, 1, 5, and 10 mg mL^{-1} OA-Fe_3O_4 NP solutions, respectively. (c) Volumetric capacitance of the (CNT/OA-Fe_3O_4 NP)$_n$ multilayer electrodes as a function of the adsorbed amount of OA-Fe_3O_4 NPs. The inset shows TEM images of OA-Fe_3O_4 NPs deposited onto the CNT network. (d) Capacitance retention of the (CNT/OA-Fe_3O_4 NP)$_{20}$ and (cationic CNT/anionic octakis-Fe_3O_4 NP)$_{20}$ multilayer electrodes as a function of cycling number (n) at a constant scan rate of 100 mV s^{-1}.

69 F cm^{-3} at 5 mV s^{-1}, respectively. Although the specific capacitance value (79 F $\cdot g^{-1}$) of the OA-Fe_3O_4 NPs used in our study is significantly lower than that of other transition metal oxide (TMO) NPs, such as MnO_2 (1370 F $\cdot g^{-1}$; this high capacitance value can theoretically only be achieved for ultrathin films or nanoparticles) or RuO_2 (720-900 F $\cdot g^{-1}$) in acidic electrolytes, it should be noted that the volumetric capacitance of the (CNT/OA-Fe_3O_4 NP)$_n$ film electrodes was comparable to that (246 F $\cdot cm^{-3}$) of previously reported electrostatic LbL-assembled (charged CNT multilayers/amorphous MnO_x NP) electrodes [42] and higher than that of conventional CNT-based electrodes [64,65]. These phenomena were mainly caused by the dense packing of well-defined OA-Fe_3O_4 NP arrays on the CNT layer with good access to electrons and ions in the electrolyte.

Because the loading amount (or packing density) of Fe_3O_4 NPs in the CNT network is key for determining the volumetric capacitance in a limited volume electrode, investigating the electrochemical performance as a function of the packing density of OA-Fe_3O_4 NPs can serve as a foundational path toward the development of optimized supercapacitors. To clarify these issues, we investigated the electrochemical performances of (CNT/OA-Fe_3O_4 NP)$_{20}$ electrodes prepared from different concentrations (0.1, 0.5, 1, 5, and 10 mg mL^{-1}) of OA-Fe_3O_4 NP solutions. First, as the loading amount of OA-Fe_3O_4 NPs was increased from 28 (obtained from the 0.1 mg mL^{-1} OA-Fe_3O_4 NP solution) to 78 wt. % (the 10 mg mL^{-1} OA-Fe_3O_4 NP solution), the electrical conductivity decreased from 136 to 90 S cm^{-1} due to the decreased contact area among the CNT layers not bound to OA-Fe_3O_4 NPs (Fig. 6**b**). These phenomena could also be confirmed by the electrochemical impedance spectroscopy (EIS) analysis of covalent-bonding (CNT/OA-Fe_3O_4 NP)$_n$ and traditional electrostatic (cationic CNT/anionic octakis-Fe_3O_4 NP)$_n$ electrodes (Fig. S9 **in Supporting Information**). Although electrostatic LbL multilayer electrodes exhibited relatively low equivalent-series resistances and facile electrolyte diffusion compared to those of covalent-bonding LbL multilayer electrode, the volumetric capacitance of (CNT/OA-Fe_3O_4 NP)$_n$ electrode was 1.76 times higher than that of (cationic CNT/anionic octakis-Fe_3O_4 NP)$_n$ multilayer electrode as mentioned earlier. The highest volumetric performance (248 F cm^{-3} at a scan rate of 5 mV s^{-1}) was obtained from the multilayer electrode containing the most densely packed OA-Fe_3O_4 NPs (approximately 78 wt. %) (Fig. 6**c**). The film electrodes containing 78 wt. % OA-Fe_3O_4 NPs also exhibited good rate capability, as can be observed in Fig. 5**c**. These results imply that the dense packing of 8-nm OA-Fe_3O_4 NPs, as demonstrated in our approach, can significantly improve the electrochemical performance of supercapacitor electrodes.

The long-term cycling performances of LbL-(CNT/OA-Fe_3O_4 NP)$_{20}$ and (cationic CNT/anionic octakis-Fe_3O_4 NP)$_{20}$ supercapacitors were tested over 1000 cycles at a scan rate of 100 mV s^{-1} (Fig. 6**d**). The solution concentration of OA-Fe_3O_4 and anionic octakis-Fe_3O_4 NP was adjusted to 10 mg mL^{-1} to prepare the multilayer electrodes, as mentioned previously. For the (CNT/OA-Fe_3O_4 NP)$_{20}$ films, an enhancement of approximately 1-2% of the initial capacitance (after 50 cycles) was observed; this result was attributed to the increased effective interfacial area between the electrode materials and electrolyte and to the full activation of the electrode by an increase in the reaction time [66-68]. Consequently, the high electrochemical performance of the densely packed (CNT/OA-Fe_3O_4 NP)$_{20}$ electrode was maintained until 1000 cycles with a very small performance reduction of 0.8%. However, for the (cationic CNT/anionic octakis-Fe_3O_4 NP)$_{20}$ films prepared using electrostatic interactions, an approximate 19% decay in the electrochemical performance was observed after 1000 cycles. Such a decrease may be attributed to the partial desorption of anionic Fe_3O_4 NPs that were electrostatically adsorbed onto cationic CNT under continuously applied potential cycling. These results demonstrate the excellent electrochemical stability of covalently bonded LbL-(CNT/OA-Fe_3O_4 NP)$_n$ film electrodes. Although we used Fe_3O_4 NPs with a low specific capacitance to prepare the ultrathin supercapacitor electrodes, the resulting (CNT/OA-Fe_3O_4 NP)$_n$ electrodes designed using our approach exhibited excellent energy storage performance and stability compared with other nanocomposite electrodes based on high-pseudocapacitive TMO NPs [34,35,69]. Furthermore, these results suggest the possibility that the use of TMO NPs with high theoretical capacity can induce a higher energy storage performance than that of (CNT/OA-Fe_3O_4 NP)$_n$ multilayer electrodes.

To further demonstrate this possibility, the 11 ± 1 nm-sized OA-MnO NPs with high crystallinity dispersed in toluene were used for the preparation of (CNT/OA-MnO NP)$_n$ multilayer film electrodes (Fig. 7**a and Supporting Information,** Fig. S10 and S11), and the electrochemical properties of (CNT/OA-MnO NP)$_n$ electrodes were investigated at a potential range between -0.05 and $+0.8$ V in 0.1 M K_2SO_4 solution. As demonstrated in Fig. 7**b**, these film electrodes also showed a good rate capability in the range from 5 to 400 mV s^{-1}. In particular, the volumetric capacitance of the (CNT/OA-MnO NP)$_{20}$ electrodes was measured to be 305 ± 10 F cm^{-3} (183 ± 5 F g^{-1}) at a scan rate of 5 mV s^{-1}, which was superior to that of the (CNT/OA-Fe_3O_4 NP)$_{20}$ (i.e., 248 F cm^{-3} at scan rate of 5 mV s^{-1}) and the electrostatic LbL-assembled (charged CNT multilayers/amorphous MnO_x NP) supercapacitor electrodes (i.e., 246 F cm^{-3} at scan rate of 5 mV s^{-1}) [42], as well as the H-bonded (CNT/CNT)$_{20}$ electrodes (i.e., 69 F cm^{-3} at 5 mV s^{-1}) (Fig. 7**c and Supporting Information,** Fig. S12). Additionally, the (CNT/OA-MnO NP)$_{20}$ multilayer electrodes also exhibited excellent performance stability during CV operation (Fig. 7**d**). A slight increase (approximately 110%) of the initial capacitance of electrode after 1100 cycles was observed, which was almost consistent with the phenomenon observed in Fig. 6**d.** Other research groups also reported that the capacitance of manganese oxide-based electrode was increased compared to its initial capacitance during the electrochemical cycling test [70-72]. Additionally, Wang et al. reported that the specific capacitance of MnO@mesoporous carbon nanocomposite electrodes increase up to $\sim$110% of their original capacitance value after 2500 cycles [73]. They also suggested that such a slight increase of capacitance during the cycling test was ascribed to the activation effect of electrode through increasing the contact area between the electrode and electrolyte during electrochemical cycling. However, as the cycling test of the (CNT/OA-MnO NP)$_{20}$ multilayer electrode was carried out up to 10,000 cycles, the capacitance retention was gradually decreased from 110 (at 1100 cycles) to 106% of initial capacitance.

Conclusions

In conclusion, we demonstrated that high-performance ultrathin supercapacitor electrodes could be successfully prepared using direct covalent-bonding (i.e., ligand-exchange) LbL-

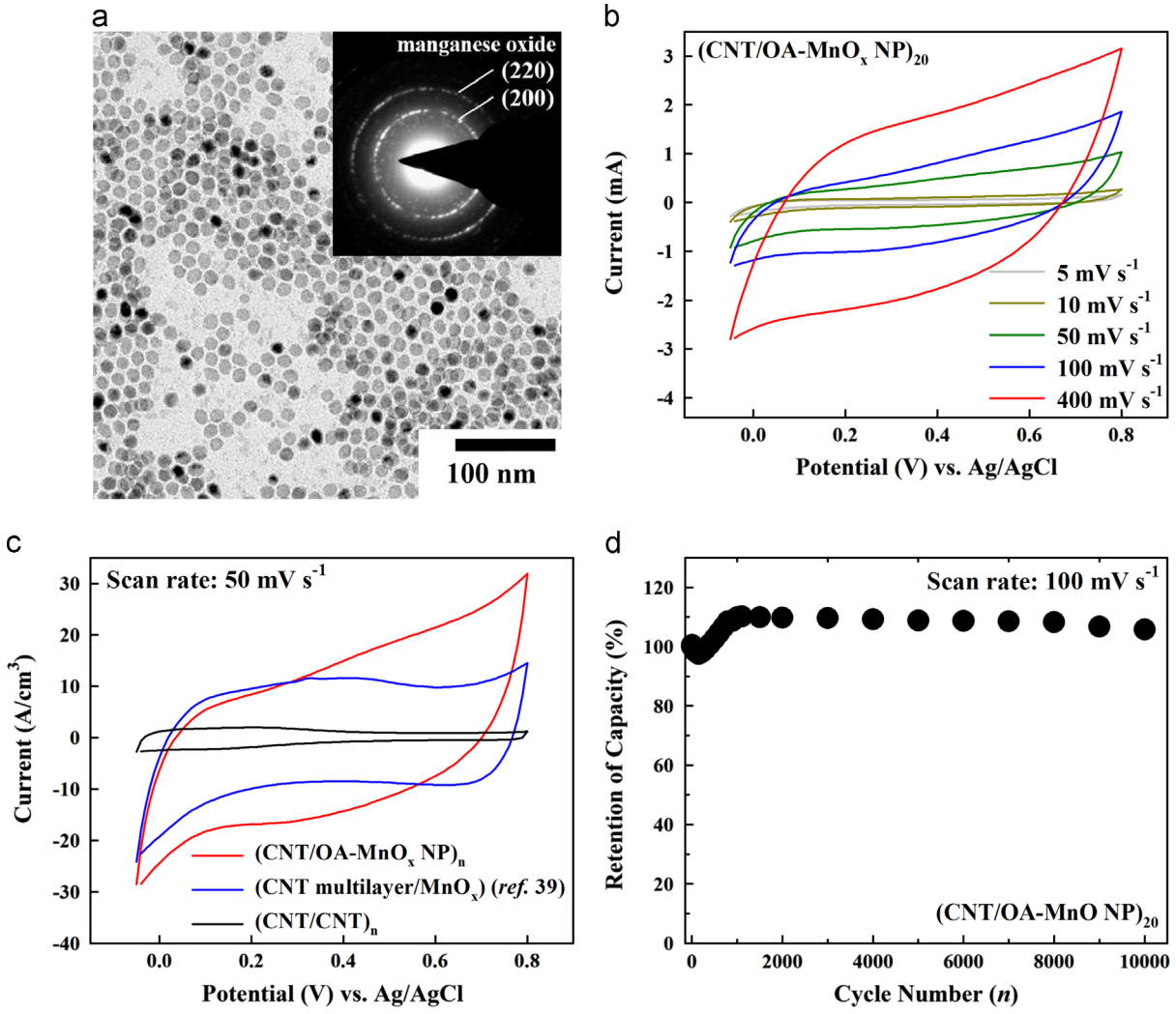

Fig. 7 (a) HR-TEM images and SAED pattern (inset) of 11 ± 1 nm-sized OA-MnO NPs. (b) Cyclic voltammograms of (CNT/OA-MnO NP)$_{20}$ as a function of scan rate from 5 to 400 mV s^{-1}. (c) Comparison of the electrochemical performance of (CNT/OA-MnO NP)$_n$ multilayer electrode with LbL-assembled CNT multilayers/amorphous MnO_x electrodes from ref. [42] at scan rage of 50 mV s^{-1}. In this case, the performance of the (CNT/OA-MnO NP)$_n$ multilayer electrodes prepared by our approach was approximately 34% higher than that of previously reported one in ref. [42]. (d) Cycling stability of (CNT/OA-MnO NP)$_n$ multilayer electrodes as a function of cycle number (n) at a constant scan rate of 100 mV s^{-1}.

assembled films composed of CNT and highly crystalline TMO NPs in organic media. In particular, the direct adsorption of densely packed OA-TMO NP arrays on the porous CNT network structure without the aid of additional polymer binders or insulating materials enabled fast electrolyte ion and electron transport throughout the electrode matrix with a high surface area and the comprehensive utilization of pseudo- and double-layer capacitance, resulting in excellent electrochemical performance. Considering that our approach has notable advantages over the realization of a highly uniform nanoarchitecture, chemically stable adsorption between the active components, and facile insertion of pseudocapacitive NPs with high qualities into the films, we believe that our strategy will provide a basis for preparing ultrathin supercapacitor electrodes with high energy densities and remarkable operational stabilities.

Acknowledgments

This work was supported by NRF grant funded by the Ministry of Science, ICT & Future Planning (MSIP) (2010-0029106).

Appendix A. Supporting information

Supplementary data associated with this article can be found in the online version at http://dx.doi.org/10.1016/j.nanoen.2015.01.002.

References

[1] E. Peled, A. Gorenshtein, M. Segal, Y. Sternberg, J. Power Source 26 (1989) 269–271.

[2] A.S. Arico, P. Bruce, B. Scrosati, J.-M. Tarascon, W.V. Schalkwijk, Nat. Mater. 4 (2005) 366–377.
[3] A. Marschilok, C.-Y. Lee, A. Subramanian, K.J. Takeuchi, E.S. Takeuchi, Energy Environ. Sci 4 (2011) 2943–2951.
[4] A.R. Park, J.S. Kim, K.S. Kim, K. Zhang, J. Park, J.H. Park, J.K. Lee, P.J. Yoo, ACS Appl. Mater. Interface 6 (2014) 1702–1708.
[5] H. Xia, Y. Wan, L. Lu, Mater. Chem. Phys. 143 (2014) 720–727.
[6] S. Park, J.M. Vohs, R.J. Gorte, Nature 404 (2000) 265–267.
[7] B.C.H. Steele, A. Heinzel, Nature 414 (2001) 345–352.
[8] S. Tominaka, H. Nishizeko, J. Muzuno, T. Osaka, Energy Environ. Sci 2 (2009) 1074–1077.
[9] J.R. Miller, P. Simon, Science 321 (2008) 651–652.
[10] P. Simon, Y. Gogotsi, Nat. Mater. 7 (2008) 845–854.
[11] H.-S. Park, M.-H. Lee, R.Y. Hwang, O.-K. Park, K. Jo, T. Lee, B.-S. Kim, H.-K. Song, Nano Energy 3 (2014) 1–9.
[12] P. Wen, P. Gong, Y. Mi, J. Wang, S. Yang, RSC Adv 4 (2014) 35914–35918.
[13] S.W. Zhang, G.Z. Chen, Energy Mater 3 (2008) 1384–1404.
[14] W. Wei, X. Cui, W. Chen, D.G. Ivey, Chem. Soc. Rev. 40 (2011) 1697–1721.
[15] E. Frackowiak, Phys. Chem. Chem. Phys. 9 (2007) 1774–1785.
[16] L. Lai, H. Yang, L. Wang, B.K. Teh, J. Zhong, H. Chou, L. Chen, W. Chen, Z. Shen, R.S. Ruoff, J. Lin, ACS Nano 6 (2012) 5941–5951.
[17] J.J. Xu, K. Wang, S.Z. Zu, B.H. Han, Z.X. Wei, ACS Nano 4 (2010) 5019–5026.
[18] H.L. Wang, Q.L. Hao, X.J. Yang, L.D. Lu, X.A. Wang, Nanoscale 2 (2010) 2164–2170.
[19] K. Zhang, L.L. Zhang, X.S. Zhao, J.S. Wu, Chem. Mater. 22 (2010) 1392–1402.
[20] A.K. Mishra, S. Ramaprabhu, J. Phys. Chem. C 115 (2011) 14006–14013.
[21] A. Al-zubaidi, T. Inoue, T. Matsushita, Y. Ishii, T. Hashimoto, S. Kawasaki, J. Phys. Chem. C 116 (2012) 7681–7686.
[22] T. Hiraoka, A. Izadi-Najafabadi, T. Yamada, D.N. Futaba, S. Yasuda, O. Tanaike, H. Hatori, M. Yumura, S. Iijima, K. Hata, Adv. Funct. Mater. 20 (2010) 422–428.
[23] C. Emmenegger, P. Mauron, P. Sudan, P. Wenger, V. Hermann, R. Gallay, A. Zuttel, J. Power Source 124 (2003) 321–329.
[24] X. Dong, L. Wang, D. Wang, C. Li, J. Jin, Langmuir 28 (2012) 293–298.
[25] L. Hu, W. Chen, X. Xie, N. Liu, Y. Yang, H. Wu, Y. Yao, M. Pasta, H.N. Alshareef, Y. Cui, ACS Nano 5 (2011) 8904–8913.
[26] I.E. Rauda, V. Augustyn, B. Dunn, S. Tolbert, Acc. Chem. Res. 46 (2013) 1113–1124.
[27] P. Ragupathy, D.H. Park, G. Campet, H.N. Vasa, S.J. Hwang, J.-H. Choy, N. Munichandraiah, J. Phys. Chem. C 113 (2009) 6303–6309.
[28] Y. Jiang, P. Wang, X. Zang, Y. Yang, A. Kozinda, L. Lin, Nano Lett. 13 (2013) 3524–3530.
[29] X. Zhang, W. Shi, J. Zhu, D.J. Kharistal, W. Zhao, B.S. Lalia, H.H. Hng, Q. Yan, ACS Nano 5 (2011) 2013–2019.
[30] C. Peng, S. Zhang, X. Zhou, G.Z. Chen, Energy Environ. Sci. 3 (2010) 1499–1502.
[31] D. Lee, M.F. Rubner, R.E. Cohen, Nano Lett. 6 (2006) 2305–2312.
[32] S. Sun, Adv. Mater. 18 (2006) 393–403.
[33] J. Park, K. Ah, Y. Hwang, J.-G. Park, H.-J. Noh, J.-H. Park, N.-M. Hwangand, T. Hyeon, Nat. Mater. 3 (2004) 891–895.
[34] Z. Chen, V. Augustyn, J. Wen, Y. Zhang, M. Shen, B. Dunn, Y. Lu, Adv. Mater. 23 (2011) 791–795.
[35] R.B. Rakhi, W. Chen, D. Cha, H.N. Alshareef, J. Mater. Chem. 21 (2011) 16197–16204.
[36] F. Caruso, R.A. Caruso, Science 282 (1998) 1111–1114.
[37] P. Podsiadlo, A.K. Kaushik, E.M. Arruda, A.M. Waas, B.S. Shim, J.D. Xu, H. Nandivada, B.G. Pumplin, J. Lahann, A. Ramamoorthy, N.A. Kotov, Science 318 (2007) 80–83.
[38] G. Decher, Science 277 (1997) 1232–1237.
[39] Y. Kim, K. Kook, S.K. Hwang, C. Park, J. Cho, ACS Nano 8 (2014) 2419–2430.
[40] M. Yoon, Y. Kim, J. Cho, ACS Nano 5 (2011) 5417–5426.
[41] Y. Ko, H. Baek, Y. Kim, M. Yoon, J. Cho, ACS Nano 7 (2013) 143–153.
[42] S.W. Lee, J. Kim, S. Chen, P.T. Hammond, Y. Shao-Horn, ACS Nano 4 (2010) 3889–3896.
[43] M.N. Hyder, B.N. Gallant, N.J. Shah, Y. Shao-Horn, Nano Lett. 13 (2013) 4610-4619.
[44] K.C. Grabar, K.J. Allison, B.E. Baker, R.M. Bright, K.R. Brown, R.G. Freeman, A.P. Fox, C.D. Keating, M.D. Musick, M.J. Natan, Langmuir 12 (1996) 2353–2361.
[45] J. Schmitt, G. Decher, W.J. Dressick, S.L. Brandow, R.E. Geer, R. Shashidhar, J.M. Calvert, Adv. Mater. 9 (1997) 61–65.
[46] Z.L. Wang, Nano Today 5 (2010) 512–514.
[47] J.P. Zheng, P.J. Cygan, T.R. Jow, J. Electrochem. Soc. 142 (1995) 2699–2703.
[48] M. Toupin, T. Brousse, J.W. Long, Electrochem. Soc. Interface 17 (2008) 49–52.
[49] X. Du, C. Wang, M. Chen, Y. Jiao, J. Wang, J. Phys. Chem. C 113 (2009) 2643–2646.
[50] L. Zhang, R. He, H.-C. Gu, Appl. Surf. Sci. 253 (2006) 2611–2617.
[51] S. Yu, G.M. Chow, J. Mater. Chem. 14 (2004) 2781–2786.
[52] T. Ramanathan, F.T. Fisher, R.S. Ruoff, L.C. Brinson, Chem. Mater. 17 (2005) 1290–1295.
[53] F. Su, C. Lu, H.-S. Chen, Langmuir 27 (2011) 8090–8098.
[54] D. Yoo, S.S. Shiratori, M.F. Rubner, Macromolecules 31 (1998) 4309–4318.
[55] J. Cho, K. Char, Langmuir 20 (2004) 4011–4016.
[56] A. Mamedov, J. Ostrander, F. Aliev, N.A. Kotov, Langmuir 16 (2000) 3941–3949.
[57] P. Poddar, T. Telem-Shafir, T. Fried, G. Markovich, Phys. Rev. B 66 (2002) 060403.
[58] R. Li, X. Ren, F. Zhang, C. Du, J. Liu, Chem. Commun. 48 (2012) 5010–5012.
[59] T.H. Kim, E.Y. Jang, N.J. Lee, D.J. Choi, K.-J. Lee, J.-T. Jang, J.-S. Choi, S.H. Moon, J. Cheon, Nano Lett. 9 (2009) 2229–2233.
[60] S. Kim, Y. Kim, Y. Ko, J. Cho, J. Mater. Chem. 21 (2011) 8008–8013.
[61] J. Mu, B. Chen, Z. Guo, M. Zhang, P. Zhang, C. Shao, Y. Liu, Nanoscale 3 (2011) 5034–5040.
[62] K. Kuratani, K. Tatsumi, N. Kuriyama, Cryst. Growth Des. 7 (2007) 1375–1377.
[63] N.-L. Wu, S.-Y. Wang, C.-Y. Han, D.-S. Wu, L.-R. Shiue, J. Power Source 113 (2003) 173–178.
[64] J.H. Kim, K.-W. Nam, S.B. Ma, K.B. Kim, Carbon 44 (2006) 1963–1968.
[65] R.Z. Ma, J. Liang, B.Q. Wei, B. Zhang, C.L. Xu, D.H. Wu, J. Power Source 84 (1999) 126–129.
[66] Z. Fan, J. Yan, L. Zhi, Q. Zhang, T. Wei, J. Feng, M. Zhang, W. Qian, F. Wei, Adv. Mater. 22 (2010) 3723–3728.
[67] C. Yuan, J. Li, L. Hou, X. Zhang, L. Shen, X.W.D. Lou, Adv. Funct. Mater. 22 (2012) 4592–4597.
[68] C. Long, T. Wei, J. Yan, L. Jiang, Z. Fan, ACS Nano 7 (2013) 11325-11332.
[69] S. Chen, J. Zhu, X. Wu, Q. Han, X. Wang, ACS Nano 4 (2010) 2822–2830.
[70] H. Xia, D. Zhu, Z. Luo, Y. Yu, X. Shi, G. Yua, J. Kie, Sci. Rep 3 (2013) 2978.
[71] S.-C. Pang, M.A. Anderson, T.W. Chapman, J. Electrochem. Soc. 147 (2000) 444–450.
[72] J. Yan, E. Khoo, A. Sumboja, P.S. Lee, ACS Nano 4 (2010) 4147–4255.
[73] T. Wang, Z. Peng, Y. Wang, J. Tang, G. Zheng, Sci. Rep. 3 (2013) 2693.

Yongmin Ko is a Ph. D candidate under Prof. Jinhan Cho at Department of Chemical and Biological Engineering in Korea University. Currently, his research interest has focused on energy storage devices (particularly, supercapacitors and batteries) based on layer-by-layer assembled carbonaceous materials/metal oxide nanoparticles multilayer electrodes.

Dongyeeb Shin is a Ph. D candidate under Prof. Jinhan Cho at Department of Chemical and Biological Engineering in Korea University. He has focused on surface chemistry and synthesis of advanced electrode nanomaterials (especially metal oxide and carbon nanotube) for high-performance supercapacitor devices.

Bonkee Koo is a Ph. D candidate under Prof. Jinhan Cho at Department of Chemical and Biological Engineering in Korea University. He performed master course research on the fabrication of nonvolatile memory devices through layer-by-layer assembly. He has currently focused on studying a variety next generation photovoltaic materials such as hybrid organic-inorganic materials and semiconductor nanoparticles.

Dr. Seung Woo Lee is an assistant professor of the Woodruff School of Mechanical Engineering at Georgia Institute of Technology. Dr. Lee has expertise in electrode materials and electrochemical measurement techniques for energy storage and conversion devices, including rechargeable batteries, supercapacitors, fuelcells, and electrolyzers. Dr. Lee has focused on studying surface chemistry and electronic structure of various electrode materials, such as carbon nanotubes, graphenes, and metal (oxide) nanoparticles, correlating with their electrochemical properties.

Dr. Won-Sub Yoon is a professor at Department of Energy Science in Sungkyunkwan University (SKKU). He received his Ph.D. in materials science and engineering from Yonsei University, Korea. He worked at Brookhaven National Laboratory as a principal investigator and Kookmin University as a faculty member. His research group has focused on electrode materials and structural properties for energy conversion and storage systems including rechargeable batteries, fuel cells, and supercapacitors.

Dr. Jinhan Cho is an associate professor at the Department of Chemical & Biological Engineering in Korea University. Dr. Cho has expertise in the surface modification of metal or metal oxide nanoparticles as well as the layer-by-layer assembled functional multilayers including optical films, nonvolatile memory devices, electrochemical sensors, energy harvesting/storage devices. Dr. Cho has now focused on studying surface chemistry and electrochemical properties of various electrode materials, such as carbon nanotubes, graphenes, conducting polymers, and metal (or metal oxide) nanoparticles.